Post-Print

This is the accepted version of:

The final publication is available at https://doi.org/10.1016/j.ijheatmasstransfer.2021.122114

Access to the published version may require subscription.

When citing this work, cite the original published paper.

Permanent link to this version
http://hdl.handle.net/11311/1188786

Highlights:

1. analytical method to predict the thermal behavior of multi-source multi-layer compound systems;

2. reduction of total component resistance is obtained through optimal apportionment of layer thicknesses;

3. anisotropic materials allow limited substrate thickness, but at an expected high cost;

4. for single-source systems, the objective function reduces to the minimum total resistance of the compound system;

5. for multi-source systems, the objective function aims at minimizing the peak temperature on top surface.

A Fast Computational Method for the Optimal Thermal Design of Anisotropic Multilayer Structures with Discrete Heat Sources for Electrified Propulsion Systems

F. Ghioldi*,a, J. Hèlieb, F. Piscagliaa

aDept. of Aerospace Science and Technology (DAER), Politecnico di Milano, Italy

bVitesco Technologies, Toulouse, France

Abstract

This work investigates the effect of the anisotropy on the heat transfer properties of layered composite materials with discrete heat sources, that are used in the power electronics of hybrid-electric propulsion systems. An analytical method, based on closed-form expressions structured on Fourier expansion series, is proposed for the solution of the Laplace's steady-state anisotropic heat equation. The physical presence of electrical components is replaced by externally applied power sources. The method provides an accurate prediction of the temperature distribution and of the heat transfer across perfect layer-to-layer adhesion or finite conductance interfaces; its use is therefore encouraged for the optimization of composite substrates. Code verification has been employed on test cases for which the analytical solution was available.

Key words: electric motors, electronics cooling, anisotropic multilayer structures, spreading resistance, optimization

1. Introduction

Battery-powered electric propulsion systems are characterized by a very precise control and response time. For this reason, they are employed in various fields for numerous applications. In Aeronautics and Aerospace, they adjust the differential thrust control required to maneuver multirotor drones, fixed-wing unmanned aerial vehicles (UAVs), and Electric Vertical Takeoff and Landing (eVTOL) aircrafts. In Automotive, they embody the core technology for advanced hybrid and electric vehicles. The extensive use of microelectronic components in electric motors is resulting in a significant increase in the complexity and integration density [1, 2]. The use of new materials such as wide bandgap semiconductors based on silicon carbide (SiC) and gallium nitride (GaN) allows for greater power efficiency, smaller size, lighter weight and lower overall cost of the system [3, 4, 5], but favors highly concentrated heat fluxes in the electric motor. Anisotropic and high-conductivity composite materials are able to ensure a uniform temperature of the electronic components [6, 7] in modern cooling systems; their use as thermal spreaders for compound substrates favors a reduction of the thermal stress and thermal resistance, which are often addressed as the main indicators of thermal performance. While anisotropic and high-conductivity composite materials are widely used in Aerospace, their application in Automotive is still limited, because of the need to make electromobility possibly affordable for everybody. The most common anisotropic material in any electronic system relates to the PCB (Printed Circuit Board) including the insulator, the copper seed layers and the silicon vias. The optimal thermal design and management is essential in electric motors, to control the device peak temperature, and to preserve and ensure performance, safety and durability of the battery [8, 9]. A common application in microelectronics consists of using discrete heat sources placed on rectangular plates with convective cooling; this is done to ensure sufficient thermal dissipation to guarantee the optimum working temperature range for different components (50° C-60° C for batteries, 40° C for sensors).

---

*Corresponding authors: `federico.ghioldi@polimi.it`

Several numerical strategies for the optimal thermal design of microelectronic components have been developed through the years. The Finite Difference (FD) method and Finite Element Analysis (FEA) have proven to be reliable employments for solving heat transfer in complex geometries [2, 10, 11, 12], despite their high computational cost. On the other hand, analytical solutions based on Fourier series techniques allow for the simulation of complex thermal spreading problems in short times [13, 14, 15, 16]. These closed-form expressions for the solution of the Laplace's steady-state heat equation can untangle single or multi-layer problems concerning single or multi-component layouts; they are based on the assumption that the physical presence of electrical components is substituted by externally applied power sources [17].

A preliminary non-dimensional solution for temperature and heat flux distribution was given in [18] for a single centered component on top of a single isotropic layer. Similar non-dimensional solutions were reported in [19], for a squared component placed on top of a square substrate having fin heat promoters. A transformation of rectangular isotropic substrates into rounded flux tubes was proposed in [20], so as to reduce the number of expansion series summations and ease the procedure. Double-side cooling was investigated in [21] with convective effects accounted on both top and bottom surface of a single isotropic layer. An investigation of double isotropic layer problems with multiple eccentric components was reported in [22]. The study was subsequently extended to multi-layer systems with finite conductance at the interface in [2]. For double orthotropic layers, the analysis conducted in [23, 24] suggested a coordinate transformation so as to handle their pseudo-isotropic counterpart. Orthotropic double-layer substrates were also treated in [1, 25] where a solution was obtained for perfect adhesion and finite conductance, for single and multi-component configurations. Insulated substrates with single anisotropic layer were analyzed in [26], having sources and sinks on both sides, neglecting the heat sink convective plane. As further complication, the authors in [11, 27, 28, 29] included a vapour chamber in between isotropic laminates, in order to passively spread the heat by promoting two-phase recirculation based on capillary force pumping.

Moreover, once the temperature distribution is known in the source plane as the solution of the Laplace's heat equation, a prediction for the total resistance connected to each component can be obtained. A method to compute multi-component resistance was described in [30], by using an equivalent source area; the accuracy of the method was proven only for simplified cases. In [31], the Influence Coefficient Method was proposed to accurately characterize the thermal resistance in multi-component configurations, where interactions among sources were present. An alternative method to predict the heat spreading effects due to boundary heat sources, based on the computation of a spreading cone angle, was described in [32]. All the mentioned methods are able to simulate the complete substrate behavior at a very limited computational cost, so they are suitable to be embedded within an optimization procedure. The authors in [33] showed an optimization procedure based on the manipulation of the isotropic form of the single-layer solutions to extract non-dimensional parameters. In [34] the optimization of high conductivity single layer substrates brought to a simplified equation for the reliable prediction of the optimal layer thickness for high component-to-base surface ratios only.

The purpose of this work is to develop a fast reliable algorithm for the prediction of the temperature distribution and of the thermal resistance of chips and devices mounted on substrates, that are convectively cooled on the bottom surface [19, 35, 36]. Semi-empirical correlations are used to estimate the convective heat transfer coefficient and to account for uniform and non-uniform cooling of the pack [37, 38, 39, 40, 41]. The theory has been implemented in an in-house numerical tool, that has been applied for the thermal optimization of the substrate. The tool identifies the best configuration within bounded regions of admissibility, by varying the geometrical parameters of the substrate in an automatic fashion. The paper is organized as follows: the analytical solution for the temperature rise is presented in Sec. 2 for isotropic, orthotropic, and anisotropic compound systems with perfect layer adhesion and finite layer-to-layer conductance. The analytical method described in Sec. 2 is applied in Sec. 3 for the characterization of the total resistance of single- and multi-layer structures, with single or multiple heating components. A procedure for the optimal design of the multi-layer system is described in Sec. 4. Code verification is performed in Sec. 5 against test cases available from the literature [1, 22, 25]. Three-dimensional multi-region simulations [42, 43] are used in Sec. 6 to assert the quality of the optimization process. Conclusions are drawn in Sec. 7.

2. Calculation of the temperature distribution in multi-layer structures

The baseline multi-layer single heat source system studied in this work (Fig. 1) features N substrate layers, that are characterized by a thickness t_j and by an anisotropic conductivity $\boldsymbol{k}_j$. N_c electronic components ($N_c = 1$ in Fig. 1) are installed on the upper surface of the system; each component, whose dimensions are L_c and W_c, generates a heat flux q and a heat power $Q = q\,A_c$ through its contact surface A_c.

For the anisotropic multi-layer substrate of Fig. 1, the steady-state heat conduction equation is used to calculate the steady-state temperature distribution:

$$\nabla \cdot (k\nabla T) = k_x \frac{\partial^2 T}{\partial x^2} + k_y \frac{\partial^2 T}{\partial y^2} + k_z \frac{\partial^2 T}{\partial z^2} = 0 \tag{1}$$

Being the excess temperature defined as:

$$\theta(x, y, z) = T - T_{amb} \tag{2}$$

a variable substitution can be applied to Eq. 1, that takes the form:

$$\frac{\partial^2 \theta}{\partial x^2} + \frac{k_y}{k_x} \frac{\partial^2 \theta}{\partial y^2} + \frac{k_z}{k_x} \frac{\partial^2 \theta}{\partial z^2} = 0 \tag{3}$$

On the source plane of Fig. 1, the following boundary conditions are applied:

$$\left. \frac{\partial \theta_1}{\partial z} \right|_{z_1=0} = 0 \qquad (x, y) \in (A_{base} - A_c) \tag{4}$$

$$-k_{z,1} \left. \frac{\partial \theta_1}{\partial z} \right|_{z_1=0} = q \qquad (x, y) \in A_c \tag{5}$$

while for the adiabatic side walls of the structure it holds:

$$\left. \frac{\partial \theta}{\partial x} \right|_{x=0} = \left. \frac{\partial \theta}{\partial x} \right|_{x=L} = \left. \frac{\partial \theta}{\partial y} \right|_{y=0} = \left. \frac{\partial \theta}{\partial y} \right|_{y=W} = 0 \tag{6}$$

and for the N-th layer:

$$\left. \frac{\partial \theta_N}{\partial z} \right|_{z_N=t_N} = -\frac{\bar{h}}{k_{z,N}} \theta_N(x, y, t_N) \tag{7}$$

The average heat transfer coefficient $\bar{h}$ is assumed to be constant over the bottom surface of the N-th layer and it is defined as:

$$\bar{h} = \frac{1}{A_{base}} \int_{A_{base}} h(x, y) dA \tag{8}$$

Using the separation of variables, the solution of Eq. 3 written in terms of Fourier expansion series is:

$$\theta = \sum_{m=1}^{\infty} \sum_{n=1}^{\infty} C(\lambda, \delta) e^{\lambda x} e^{\delta\left(\sqrt{k_x/k_y}\right)y} e^{i\sqrt{\lambda^2 + \delta^2}\left(\sqrt{k_x/k_z}\right)z} \tag{9}$$

If the adiabatic boundary conditions (Eq. 6) are applied to Eq. 9 it follows:

$$
\begin{aligned}
\theta =\ & A_{00} + B_0 \sqrt{\frac{k_x}{k_z}} z \\
& + \sum_{m=1}^{\infty} \cos(\lambda_m x) \left[A_m \cosh\left(\lambda_m \sqrt{\frac{k_x}{k_z}} z\right) + B_m \sinh\left(\lambda_m \sqrt{\frac{k_x}{k_z}} z\right) \right] \\
& + \sum_{n=1}^{\infty} \cos\left(\delta_n \sqrt{\frac{k_x}{k_y}} y\right) \left[A_n \cosh\left(\delta_n \sqrt{\frac{k_x}{k_z}} z\right) + B_n \sinh\left(\delta_n \sqrt{\frac{k_x}{k_z}} z\right) \right] \\
& + \sum_{m=1}^{\infty} \sum_{n=1}^{\infty} \cos(\lambda_m x) \cos\left(\delta_n \sqrt{\frac{k_x}{k_y}} y\right) \left[A_{mn} \cosh\left(\beta_{mn} \sqrt{\frac{k_x}{k_z}} z\right) + B_{mn} \sinh\left(\beta_{mn} \sqrt{\frac{k_x}{k_z}} z\right) \right]
\end{aligned} \tag{10}
$$

4

for which $\lambda_m = \dfrac{m\pi}{L}$, $\delta_n = \dfrac{n\pi}{W}\sqrt{\dfrac{k_y}{k_x}}$ and $\beta_{mn} = \sqrt{\lambda_m^2 + \delta_n^2}$. In Eq. 10, substrate layers can be isotropic ($k_x = k_y = k_z$, see Appendix A), orthotropic ($k_x = k_y = k_{ip} \neq k_z$, see Appendix B), or anisotropic ($k_x \neq k_y \neq k_z$). If Eq. 7 is combined with Eq. 10, under the assumption of anisotropic solid, it follows:

$$B_0 = -\left(\frac{\bar{h}}{k_{z,N} + \bar{h}t_N}\right)\sqrt{\frac{k_{z,N}}{k_{x,N}}}\, A_{00} \tag{11}$$

$$B_{i,N} = -\underbrace{\left(\frac{\bar{h} + k_{z,N}\gamma\sqrt{\frac{k_{x,N}}{k_{z,N}}}\tanh\left(\gamma\sqrt{\frac{k_{x,N}}{k_{z,N}}}t_N\right)}{\bar{h}\tanh\left(\gamma\sqrt{\frac{k_{x,N}}{k_{z,N}}}t_N\right) + k_{z,N}\gamma\sqrt{\frac{k_{x,N}}{k_{z,N}}}}\right)}_{\Phi_N(\gamma)} A_{i,N} \tag{12}$$

where $\gamma = \lambda_m$, δ_n, β_{mn} for $B_i = B_m$, B_n, B_{mn} respectively, and $\Phi_N(\gamma)$ is the spreading function for the bottom layer N.

System closure is achieved by the boundary conditions to model layer-to-layer interfaces, that can be based on the assumption of *perfect adhesion* (Sec. 2.1) or of *finite conductance* (Sec. 2.2) between the layers.

2.1. Perfect adhesion at the layer-to-layer interface

For the layer $j \in [1 : N-1]$ of Fig. 1, the assumption of *perfect adhesion* is:

$$\theta_j\left(x,y,z_j=t_j\right) = \theta_{j+1}\left(x,y,z_{j+1}=0\right) \tag{13}$$

$$k_{z,j}\left.\frac{\partial\theta_j}{\partial z}\right|_{z_j=t_j} = k_{z,j+1}\left.\frac{\partial\theta_{j+1}}{\partial z}\right|_{z_{j+1}=0} \tag{14}$$

Combining Eq. 10 with 13 and 14, it follows:

$$B_{i,j} = -\underbrace{\left(\frac{\tanh\left(\gamma\sqrt{\frac{k_{x,j}}{k_{z,j}}}t_j\right) + \Phi_{j+1}(\gamma)\sqrt{\frac{k_{z,j+1}}{k_{z,j}}}\sqrt{\frac{k_{x,j+1}}{k_{x,j}}}}{1 + \Phi_{j+1}(\gamma)\sqrt{\frac{k_{z,j+1}}{k_{z,j}}}\sqrt{\frac{k_{x,j+1}}{k_{x,j}}}\tanh\left(\gamma\sqrt{\frac{k_{x,j}}{k_{z,j}}}t_j\right)}\right)}_{\Phi_j(\gamma)} A_{i,j} \tag{15}$$

where $\Phi_j(\gamma)$ is the spreading function for the layer j.

An iterative procedure on Eq. 12 and Eq. 15 must be employed to obtain the temperature distribution on the heated surface [2]. It is then possible from Eq. 5 to calculate the coefficients A_i:

$$A_{00} = \frac{Q}{LW}\left(\sum_{j=1}^{N}\frac{t_j}{k_{z,j}} + \frac{1}{\bar{h}}\right) \tag{16}$$

$$A_m = \sum_{m=1}^{\infty}\frac{4Q\cos\left(\lambda_m X_c\right)\sin\left(\lambda_m\frac{L_c}{2}\right)}{LWL_c\, k_{z,j}\lambda_m^2\Phi(\lambda)\sqrt{\frac{k_{x,j}}{k_{z,j}}}} \tag{17}$$

$$A_n = \sum_{n=1}^{\infty}\frac{4Q\cos\left(\delta_n\sqrt{\frac{k_{x,j}}{k_{y,j}}}Y_c\right)\sin\left(\delta_n\sqrt{\frac{k_{x,j}}{k_{y,j}}}\frac{W_c}{2}\right)}{LWW_c\, k_{z,j}\delta_n^2\Phi(\delta)\sqrt{\frac{k_{x,j}}{k_{z,j}}}\sqrt{\frac{k_{x,j}}{k_{y,j}}}} \tag{18}$$

$$A_{mn} = \sum_{m=1}^{\infty}\sum_{n=1}^{\infty}\frac{16Q\cos\left(\lambda_m X_c\right)\cos\left(\delta_n\sqrt{\frac{k_{x,j}}{k_{y,j}}}Y_c\right)\sin\left(\lambda_m\frac{L_c}{2}\right)\sin\left(\delta_n\sqrt{\frac{k_{x,j}}{k_{y,j}}}\frac{W_c}{2}\right)}{LWL_cW_c\, k_{z,j}\,\lambda_m\delta_n\beta_{mn}\,\Phi(\beta)\sqrt{\frac{k_{x,j}}{k_{z,j}}}\sqrt{\frac{k_{x,j}}{k_{y,j}}}} \tag{19}$$

In case of forced convection along x-direction, a wake effect can be considered, and $A_{00}^* = A_{00} + \frac{Q}{\dot{m}c_p}\frac{x}{L}$ [22]. With multi-component configurations (Fig. 1c), the superimposition of effects holds [1]:

$$\theta = \sum_{i=1}^{N_c} \theta_i. \tag{20}$$

2.2. Finite conductance at the layer-to-layer interface

If the assumption of *finite conductance* is applied at the layer interfaces (Fig. 1f), the new set of boundary conditions for the layer $j \in [1 : N-1]$ is:

$$k_{z,j}\left.\frac{\partial\theta_j}{\partial z}\right|_{z_j=t_j} = k_{z,j+1}\left.\frac{\partial\theta_{j+1}}{\partial z}\right|_{z_{j+1}=0} \tag{21}$$

$$-k_{z,j}\left.\frac{\partial\theta_j}{\partial z}\right|_{z_j=t_j} = h_{f,j}\left[\theta_j(x,y,z_j=t_j) - \theta_{j+1}(x,y,z_{j+1}=0)\right] \tag{22}$$

where $h_{f,j} = \frac{k_f}{t_f}$ is the finite plane-to-plane conductance between layer j and $j+1$. The thickness t_f of the contact material is usually very small, and k_f is typically isotropic. The anisotropic spreading function $\Phi_j(\gamma)$ for layer j is derived from the definition of the Fourier coefficient:

$$B_{i,j} = -\underbrace{\left(\frac{\frac{k_{z,j}}{k_{z,j+1}}\tanh\left(\gamma\sqrt{\frac{k_{x,j}}{k_{z,j}}}t_j\right) + \Phi_{j+1}(\gamma)\frac{k_{z,j}}{h_{f,j}}\gamma\sqrt{\frac{k_{x,j+1}}{k_{z,j+1}}}\tanh\left(\gamma\sqrt{\frac{k_{x,j}}{k_{z,j}}}t_j\right) + \Phi_{j+1}(\gamma)\sqrt{\frac{k_{x,j+1}}{k_{z,j+1}}}\sqrt{\frac{k_{z,j}}{k_{x,j}}}}{\frac{k_{z,j}}{k_{z,j+1}} + \Phi_{j+1}(\gamma)\frac{k_{z,j}}{h_{f,j}}\gamma\sqrt{\frac{k_{x,j+1}}{k_{z,j+1}}} + \Phi_{j+1}(\gamma)\sqrt{\frac{k_{x,j+1}}{k_{z,j+1}}}\sqrt{\frac{k_{z,j}}{k_{x,j}}}\tanh\left(\gamma\sqrt{\frac{k_{x,j}}{k_{z,j}}}t_j\right)}\right)}_{\Phi_j(\gamma)} A_{i,j}$$

$$\tag{23}$$

A similar iterative procedure must be employed to obtain the temperature distribution on the heated surface involving Eq. 12 and Eq. 23. For this case, A_{00} is calculated as follows:

$$A_{00} = \frac{Q}{LW}\left(\frac{1}{\bar{h}} + \sum_{j=1}^{N-1}\frac{1}{h_{f,j}} + \sum_{j=1}^{N}\frac{t_j}{k_{z,j}}\right) \tag{24}$$

The remaining A_i values (Eq. 17 to 19) are unvaried, but the spreading function $\Phi_j(\gamma)$ from Eq. 23 must be used for their evaluation. Perfect adhesion is recovered if $h_f \to \infty$. The treatment of isotropic and orthotropic cases with finite conductance at the interface is reported in Appendix A and Appendix B.

3. The Influence Coefficient Method

An alternative approach to characterize the component is by the calculation of its total resistance, that is defined as:

$$R_t = \frac{\max(\theta_1)}{Q} \tag{25}$$

where $\max(\theta_1)$ is the highest value of temperature excess in the top layer at $z_1 = 0$ (see Fig. 1), and it is calculated from Eq. 10. The in-plane location of this peak value usually corresponds to the single component centroid. The total resistance R_t can be modelled as the sum of two contributions:

$$R_t = R_{1D} + R_{sp} \tag{26}$$

where R_{1D} includes the effects of the conductive and the convective heat transfer from the substrate, and R_{sp} is the spreading resistance. R_{sp} is present whenever the heat travels from a small surface across a larger contact

region; if the component dimension corresponds to the substrate footprint ($A_c = A_{base}$), R_{sp} is zero. In multi-component configurations, Eq. 26 cannot be calculated directly for each source [22], so the Influence Coefficient Method is used [31]. The Influence Coefficient Method accounts for the heat fluxes introduced by the several sources to calculate R_t at the interface between the upper layer and the component; the temperature excess in the centroid of the s-th component is hence written as a combination of Eq. 10 with Eq. 20:

$$\theta_s = \sum_{i=1}^{N_c} \theta_i(X_{c,s}, Y_{c,s}, 0) = \sum_{i=1}^{N_c} Q_i f_{i,s} \tag{27}$$

where the heat power Q of the i-th source is multiplied by an influence coefficient $f_{i,s}$. The coefficient $f_{i,s}$ depends on the compound properties and the geometrical characteristics of the i-th component. For the s-th source, the self-effect corresponds to the case when $i = s$. Being the square matrix $[F_{is}]$ of the influence coefficients symmetric [1], Eq. 27 can be written as:

$$\begin{Bmatrix} \theta_0 \\ \theta_1 \\ \vdots \\ \theta_{N_c} \end{Bmatrix} = \begin{bmatrix} f_{0,0} & f_{0,1} & \cdots & f_{0,N_c} \\ & f_{1,1} & \cdots & f_{1,N_c} \\ & sym & \ddots & \vdots \\ & & & f_{N_c,N_c} \end{bmatrix} \begin{Bmatrix} Q_0 \\ Q_1 \\ \vdots \\ Q_{N_c} \end{Bmatrix} \qquad \{\theta_s\} = [F_{is}]\{Q_i\} \tag{28}$$

The Influence Coefficient Method provides an alternative method to calculate the total resistance of each component $R_{t,s}$ in multi-component systems:

$$R_{t,s} = \frac{\theta_s}{Q_s} = \sum_{i=1}^{N_c} \frac{Q_i}{Q_s} f_{i,s} \qquad\qquad \bar{R}_{t,s} = \frac{\bar{\theta}_s}{Q_s} = \sum_{i=1}^{N_c} \frac{Q_i}{Q_s} \bar{f}_{i,s} \tag{29}$$

The total resistance $\bar{R}_{t,s}$ can be also calculated [1, 17, 18, 23, 31] from the temperature excess of the s-th component $\bar{\theta}_s$, averaged over its area:

$$\bar{\theta}_s = \frac{1}{A_{c,s}} \iint_{A_{c,s}} \theta_s \, dA_s \tag{30}$$

where $A_{c,s} = L_{c,s} W_{c,s}$. The average temperature contribution of the i-th heat source on the s-th component (and its respective centroid position) is:

$$\bar{\theta}_s|_{z_1=0} = A_{00} + \sum_{m=1}^{\infty} A_{m,i} \frac{2\cos(\lambda_m X_{c,s})\sin\left(\lambda_m \frac{L_{c,s}}{2}\right)}{\lambda_m L_{c,s}} + \sum_{n=1}^{\infty} A_{n,i} \frac{2\cos\left(\delta_n \sqrt{\frac{k_{x,1}}{k_{y,1}}} Y_{c,s}\right)\sin\left(\delta_n \sqrt{\frac{k_{x,1}}{k_{y,1}}} \frac{W_{c,s}}{2}\right)}{\delta_n \sqrt{\frac{k_{x,1}}{k_{y,1}}} W_{c,s}}$$
$$+ \sum_{m=1}^{\infty}\sum_{n=1}^{\infty} A_{mn,i} \frac{4\cos(\lambda_m X_{c,s})\sin\left(\lambda_m \frac{L_{c,s}}{2}\right)\cos\left(\delta_n \sqrt{\frac{k_{x,1}}{k_{y,1}}} Y_{c,s}\right)\sin\left(\delta_n \sqrt{\frac{k_{x,1}}{k_{y,1}}} \frac{W_{c,s}}{2}\right)}{\lambda_m \delta_n \sqrt{\frac{k_{x,1}}{k_{y,1}}} L_{c,s} W_{c,s}} \tag{31}$$

The A_i values are presented in Eq. 16 to 19. The influence coefficient is evaluated from the combination of Eq. 27 and Eq. 31. The averaged total resistance $\bar{R}_{t,s}$ is quantified using Eq. 29 and 31. If a single component is present, only the self-effect exists, as $s = i$, and the problem reduces to Eq. 26.

4. Optimal design of the substrate

If the temperature distribution in the substrate and the total resistance R_t are known, it is possible to derive a procedure for the optimization of the thermal design of the system, to limit the peak temperature of the components. The optimization procedure may be applied either to a single layer or to the complete substrate; this can be done by the analysis of the temperature peak (or peaks), or by the calculation of the one-dimensional and spreading resistances. The total resistance R_t for a component is an indicator of the performance of the

substrate and its calculation allows to rapidly compare different configurations. The optimized total resistance $R_{t,opt}$ is obtained through minimization:

$$R_{t,opt} = \min\left(R_t\right) \tag{32}$$

For systems with a single component, a minimum in the total resistance $R_{t,opt}$ corresponds to a minimum of the peak component temperature θ_s. For multi-component systems, an objective function linked to the overall total substrate resistance may be built by the Influence Coefficient Method. This approach looks particularly suitable for configurations where there are no constraints on the component locations. As each component total resistance is influenced by the relative position of the surrounding active sources, it follows:

$$R_{t,opt} = \min\left(\sum_{i=1}^{N_c} R_{t,i}\right) \tag{33}$$

If each component position is prescribed, the solution of the problem consists of the minimization of the peak temperature of the upper surface:

$$\theta_{opt} = \min\left(\max\left(\sum_{i=1}^{N_c} \theta_i|_{z_1=0}\right)\right) \tag{34}$$

The identification of the optimal design point is often influenced by several constraints. The optimal design must account for the need to both spread and dissipate the introduced heat into the layer substrates. Besides, the minimum layer thickness is limited by the manufacturing technology, while the maximum layer thickness depends on encumbrance (E), cost (C) and weight (W). If two objective functions for cost f_C and for weight f_W respectively are defined, the maximum allowed thickness is a combination of the two contributions:

$$
\begin{aligned}
t_{j,min} &\leq t_{j,opt} \leq t_{j,max} \\
t_{j,max} &= \alpha_1 f_C + \alpha_2 f_W \\
\sum_{j=1}^{N} t_j &\leq t_{E,max}
\end{aligned}
\tag{35}
$$

In the optimization procedure, it is required the heat spreading along the three dimensions to be also maximized. The conductive heat diffusion over in-plane and cross plane directions for anisotropic composite laminates must be optimized. The anisotropic thermal conductivity has an upper bound given by cost and production capability, thus an objective funcion f_P is introduced. For each value of the thermal conductivity, an optimum thickness can be defined by Eq. 35:

$$
\begin{aligned}
\boldsymbol{k}_j &\leq \boldsymbol{k}_{j,max} \\
\boldsymbol{k}_{j,max} &= \alpha f_P \\
t_{j,opt} &= f(\boldsymbol{k}_j)
\end{aligned}
\tag{36}
$$

5. Code validation

Five cases are presented in Tab. 1 to validate the equations proposed in the previous sections. Together, they cover the entire range of combinations among number of discrete sources, nature of the substrate material (isotropic, orthotropic, anisotropic), layer-to-layer interface type. In particular, an average heat transfer coefficient $\bar{h} \to \infty$ is reported for Cases C and D in Tab. 1. This represents a constant temperature boundary condition at the bottom of the substrate. The mathematical procedure that proves this assumption is reported in Appendix C. The schematics of the tested configurations are reported in Fig. 1.
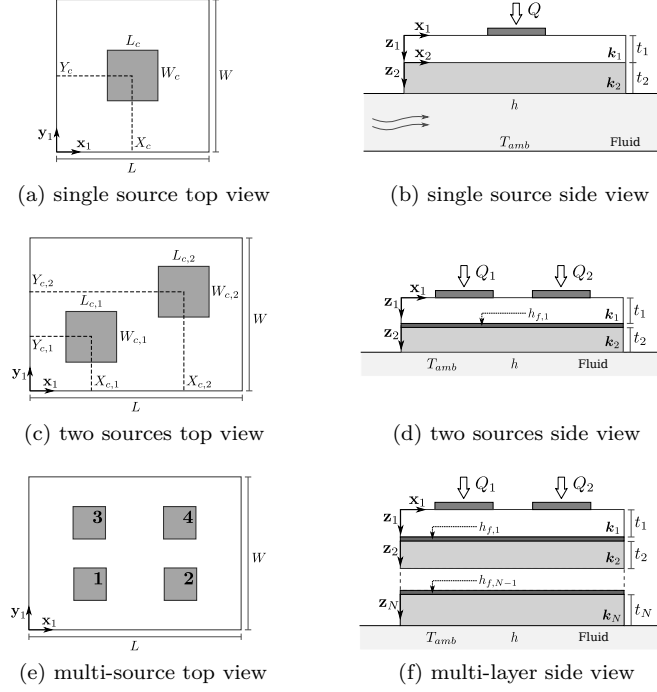
(a) single source top view

(b) single source side view

(c) two sources top view

(d) two sources side view

(e) multi-source top view

(f) multi-layer side view

Figure 1: Schematics of tested configurations; $h_{f,j}$ is the conductance between layer j and $j+1$.

	units	A [22]	B [22]	C [1]	D [1]	E [25]
N_c	[-]	2	4	1	1	1
L_c	[mm]	25	10	$0.5 \cdot 10^{-3}$	$0.5 \cdot 10^{-3}$	1
W_c	[mm]	25	10	$75 \cdot 10^{-3}$	$75 \cdot 10^{-3}$	2
$X_{c,i}$	[mm]	[90; 210]	[12.5; 37.5; 12.5; 37.5]	$25 \cdot 10^{-3}$	$25 \cdot 10^{-3}$	15
$Y_{c,i}$	[mm]	[90; 210]	[12.5; 12.5; 37.5; 37.5]	$37.5 \cdot 10^{-3}$	$37.5 \cdot 10^{-3}$	4
Q_i	[W]	[10; 15]	[10; 25; 20; 15]	0.375	0.375	2
N	[-]	2	1	2	2	3
$h_{f,j}$	[W/m²K]	perfect adh.	-	finite (Tab. 3)	finite (Tab. 4)	perfect adh.
L	[mm]	300	50	1	1	30
W	[mm]	300	50	0.35	0.35	10
$k_{x,j}$	[W/mK]	[350; 10]	150	[130; 400]	[75; 490]	[15; 10; 5]
$k_{y,j}$	[W/mK]	[350; 10]	150	[130; 400]	[75; 490]	[30; 20; 25]
$k_{z,j}$	[W/mK]	[350; 10]	150	[130; 400]	[150; 390]	[60; 80; 100]
t_j	[mm]	[2; 10]	10	$[2; 100] \cdot 10^{-3}$	$[2; 100] \cdot 10^{-3}$	[1; 2; 3]
$\bar{h}$	[W/m²K]	10	400	∞	∞	200
T_{amb}	[K]	298.15	298.15	298.15	298.15	300

Table 1: Code validation cases.

Case A. The example described in Tab. 1 shows the effects of two components on a high conductive spreader on top of a low conductivity layer. Layer substrates are isotropic and perfect layer adhesion is used to model the layer-to-layer interfaces. The results for the peak temperatures are presented in Tab. 2. Comparisons with results on the same configurations available from the literature [22] confirm the correct operation of the presented method.

Case B. The example studies the effect of a moderate conductivity single-layer substrate and four sources. Again, layer substrate is isotropic. Being the substrate made of a single layer, no layer-to-layer interfaces are present. Results of the predicted peak temperatures are reported in Tab. 2 and are in good agreement with the literature [22].

	CASE A		CASE B			
	T_1	T_2	T_1	T_2	T_3	T_4
Muzychka et Al. [22]	329.70	333.09	370.55	374.43	376.97	373.09
present	329.70	333.09	370.53	374.41	376.95	373.07

Table 2: Peak temperatures [K] of the sources with double (case A) and single (case B) layer isotropic substrate.

Case C. A test case from [1] featuring a single source on the top of a double-layer substrate is used for the validation of the finite conductance submodel applied at the layer-to-layer interface. The substrate material is assumed as isotropic (Tab. 1).

CASE C								
$h_{f,1}$ $[W/m^2K]$	10^9	$2 \cdot 10^9$	10^8	$6.67 \cdot 10^7$	$3.33 \cdot 10^7$	$2 \cdot 10^7$	10^7	$6.67 \cdot 10^6$
FEA [1]	357.92	360.07	362.44	364.58	370.10	376.21	388.38	398.22
present	357.87	360.02	362.40	364.54	370.06	376.18	388.34	398.18

Table 3: Peak temperatures [K] of the single source with a two-layer isotropic structure and finite conductance at the layer-to-layer interface. Test case from [1].

Case D. The same geometrical configuration of case C, a single source on the top of a double-layer substrate [1], is used for the validation of the finite conductance submodel applied at the layer-to-layer interface. The substrate material is now assumed as orthotropic (Tab. 1).

CASE D								
$h_{f,1}$ $[W/m^2K]$	10^9	$2 \cdot 10^9$	10^8	$6.67 \cdot 10^7$	$3.33 \cdot 10^7$	$2 \cdot 10^7$	10^7	$6.67 \cdot 10^6$
FEA [1]	362.43	365.59	369.01	372.04	379.76	388.18	404.72	417.96
present	362.38	365.54	368.96	372.00	379.72	388.13	404.68	417.92

Table 4: Peak temperatures [K] of the single source with a two-layer orthotropic structure and finite conductance at the layer-to-layer interface. Test case from [1].

Case E. Finally, a single source on top of a three-layer anisotropic substrate is used to validate the model of perfect adhesion at the layer-to-layer interface combined with the equations proposed in Sec. 2.

CASE E	
FEA [25]	394.94
present	394.95

Table 5: Source peak temperature [K]; code validation against anisotropic test case with perfect layer adhesion.

Temperature peaks predicted by the employed method show a satisfying agreement with the results from tests available from the published literature.

6. Optimal Thermal Design of Anisotropic Multilayer Substrates with Discrete Heat Sources

The optimization methodology described in Sec. 4 is here applied to the three additional test cases described in Tab. 6, namely:

- a single component on a single orthotropic layer (case F, Sec. 6.1);
- a single component on a double-layer anisotropic substrate (case G, Sec. 6.2);
- four components mounted on an anisotropic multi-layer substrate (case H, Sec. 6.3).

OPTIMIZATION CASES

	units	F	G	H
N_c	[-]	1	1	4
L_c	[mm]	18	18	$[18; 8; 15.75; 5.42]$
W_c	[mm]	15	15	$[15; 15.75; 8; 10.8]$
$X_{c,i}$	[mm]	35	35	$[24; 54; 18; 54]$
$Y_{c,i}$	[mm]	35	35	$[19; 18; 56.5; 52]$
Q_i	[W]	20	20	$[20; 10; 10; 5]$
L	[mm]	70	70	70
W	[mm]	70	70	70
$k_{x,j}$	[W/mK]	175	$[200; 1.8]$	$[30; 150]$
$k_{y,j}$	[W/mK]	175	$[390; 200]$	$[50; 200]$
$k_{z,j}$	[W/mK]	2.5	$[1.8; 390]$	$[1.8; 130]$
t_j	[mm]	1.42	$[0.94; 1]$	$[2; 5]$
$h_{f,j}$	[W/m²K]	-	∞	∞
$\bar{h}$	[W/m²K]	925.42	925.42	925.42
T_{amb}	[K]	338.15	338.15	338.15

Table 6: Optimization test cases.

6.1. Single orthotropic layer with single centered component

Case F of Tab. 6 involves a single component on the top of a single orthotropic layer substrate. Its in-plane configuration is presented in Fig. 1a. Its geometrical characteristics are noted in Tab. 6. Since the layer

is orthotropic, the conductivity $\boldsymbol{k}_1$ can be decomposed into an in-plane and a cross-plane contribution. A considerable difference is chosen between in-plane and cross-plane conductivity. Also, as shown in Fig. 1b, a channel for forced fluid convection is present below the substrate. The heat transfer coefficient of Tab. 6 is obtained from a correlation available from the literature [40]. The discrepancy with the multi-dimensional simulations is about 17% in the calculation of the heat transfer coefficient and about 0.4% for the temperature peak ($\text{err}_T \simeq 0.4\%$). The error on the temperature peak reduces to 0.1% if the same heat transfer coefficient ($\bar{h} = 925.42$ W/m^{2}K) is used in the two approaches, meaning that the error in the peak temperature is always contained. The profile of the temperature distribution on the top surface of the substrate (Fig. 2) shows the good agreement between the results of the proposed method and three-dimensional multi-region simulations used as reference. The same holds for the total component resistance, as reported in Tab. 7. The averaged total resistance in three-dimensional simulations is calculated from the averaged temperature distribution on the component projected area and it is compared with the equations proposed in Sec. 3.
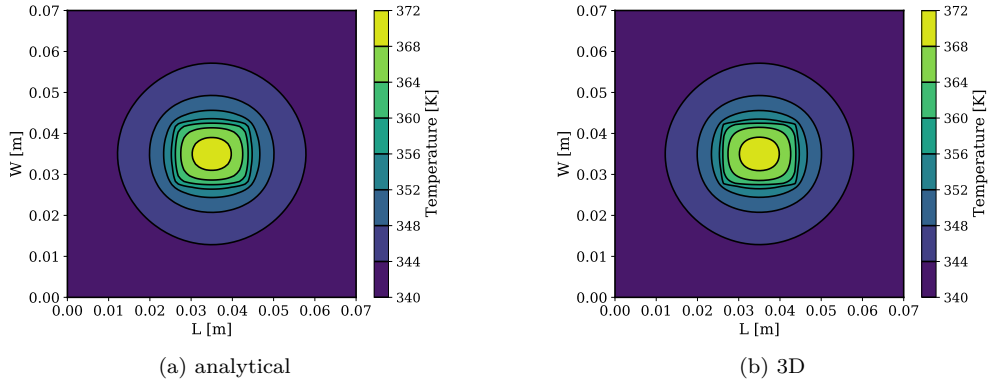

Figure 2: Case F - Isolines of temperature field [K] on top surface.

	T_1 [K]	R_t [K/W]	$\bar{R}_t$ [K/W]
analytical	370.03	1.594	1.335
3D	370.11	1.598	1.346

Table 7: Case F - Validation of the temperature peak and of the total component resistance results against solutions from three-dimensional simulations.

The temperature peak for single isolated components is located at the source centroid, as confirmed in Fig. 2. In common applications, the component size and location are input data defined by the designer; the optimization problem is applied to the definition of the optimal thickness of the substrate to improve the thermal management of the system. Following the theory of Sec. 4, the optimization of the solid layer thickness t_1 is reported in Fig. 3a. In the calculations, the constraint $t_{1,max} \leq 3$ mm is applied. The optimum point in Fig. 3a corresponds to a thickness $t_{1,opt} = 1.42$ mm (see Tab. 6). Two opposite trends for the two components of total resistance (see Eq. 26) are found; this is common when layers having high in-plane and low cross-plane thermal conductivities are used in the substrate.
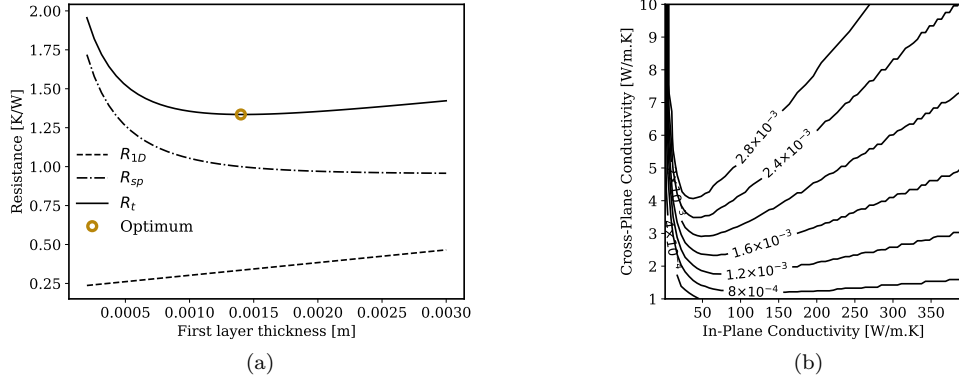
Figure 3: Case F - Minimization of total resistance by optimization of orthotropic layer thickness (a); optimal thickness for variable in-plane and cross-plane single layer conductivity (b).

This is also confirmed by Fig. 3b. For the given values of the thermal conductivity, the optimal thickness is found to be $t_{1,opt} \simeq 1.4$ mm. In Fig. 3b, for large cross-plane conductivities, the optimal layer thickness is limited by the manufacturing constraints and $t_{1,opt} = t_{1,max}$. In the other regions of the plot of Fig. 3b, the optimal value of the thickness is smaller than its upper limit; for small values of the cross-plane conductivity, large variations of the in-plane conductivity have minor effects on the optimal layer thickness (Fig. 3b). However, best practice suggests to avoid low cross-plane conductivity, because this favors an increase on the peak temperature. The latter is confirmed by the isolines of the total resistance of Fig. 4a, which also show that a small value of the total resistance of the component can be obtained with a combination of moderate cross-plane conductivity and large in-plane conductivity.
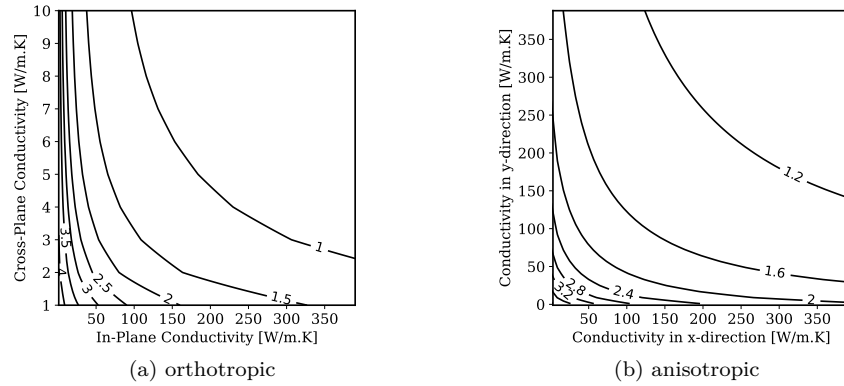

Figure 4: Case F - Total component resistance linked to optimal thickness for variable thermal conductivity (a), and for constrained cross-plane conductivity (b).

The thermal management can be improved by the use of anisotropic layers in the substrate (Fig. 4b). Different conductivities over the two in-plane directions in Fig. 4b cause non symmetric profiles of the total resistance, because of the rectangular shape of the source (Tab. 6). In fact, the geometry of the single centered heat source is the only cause of asymmetry in such a configuration, where the heat transfer coefficient $\bar{h}$ is uniform over the heat sink surface. Fig. 4b suggests that a reduction of the component peak temperature is promoted mainly by an enhancement of thermal conductivity over the y-direction. Finally, the bottom surface of the substrate can be cooled either by free or forced convection and different channel geometries can be used; for this reason, the

13

heat transfer coefficient may strongly vary from case to case. Because of the orthotropic nature of the single layer, an in-plane and a cross-plane Biot (Bi) number are calculated, that in the following will be referred as Bi_{ip} and Bi_z respectively:

$$Bi_{ip} = \frac{\bar{h}\, t}{k_{ip}} \tag{37}$$

and

$$Bi_z = \frac{\bar{h}\, t}{k_z} \tag{38}$$

Isolines for constant values of Bi_{ip} and Bi_z are reported in Fig. 5. The heat transfer coefficient range is $\bar{h} = 70 : 35000$ W/m²K for the in-plane Biot number, and $\bar{h} = 100 : 50000$ W/m²K for the cross-plane one. This is due to the fact that the heat transfer coefficient must compensate a variation of layer thickness ($t = 0.5{:}3$ mm) to preserve a constant Biot number, while the conductivity value is fixed, as prescribed in Tab. 6. Fig. 5 shows the trend of non-dimensional spreading resistance $\Psi = \frac{R_{sp}}{k\sqrt{A_{comp}}}$ for different non-dimensional thicknesses ($\tau = t/L$). Three-dimensional simulations are carried out to validate the proposed method; as shown in Fig. 5, the relative error is always lower than 0.1%.
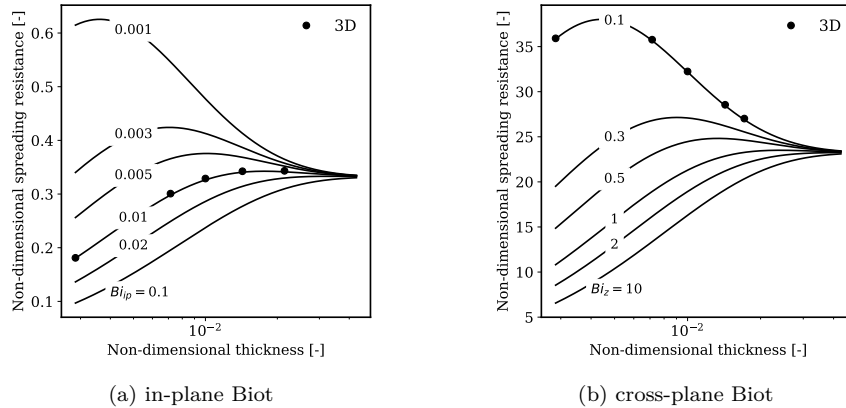

Figure 5: Case F - Non-dimensional spreading resistance at different Biot values.

In Fig. 5, isolines at constant Bi converge to a plateau for high non-dimensional thickness. When $t_N \to \infty$, the spreading function $\Phi_N(\gamma)$ tends to one and the spreading resistance R_{sp} tends to a constant value, that is independent by the heat transfer coefficient $\bar{h}$ (see Eq. 12); at the same time, the one-dimensional resistance R_{1D} increases. For thin layers ($t_N \to 0$), the heat transfer coefficient $\bar{h}$ increases, R_{sp} and R_{1D} tend to zero. The peaks of the Biot isolines are found for high values of the non-dimensional thickness, if large values of the cross-plane conductivity are used, and for low non-dimensional thicknesses when high in-plane conductivity is employed; in those regions, the non-dimensional spreading resistance is limited.

6.2. Multiple anisotropic layers with single centered component

In case G, a single centered heat source is used in combination with a substrate composed by two anisotropic layers (Fig. 1), whose characteristics are reported in Tab. 6. The temperature distribution on the upper plane is shown in Fig. 6, where the non-symmetrical in-plane behavior is also apparent. The peak temperature, the temperature distribution and total resistance predicted by the proposed method show a satisfying agreement with the three-dimensional computations (see Tab. 8).
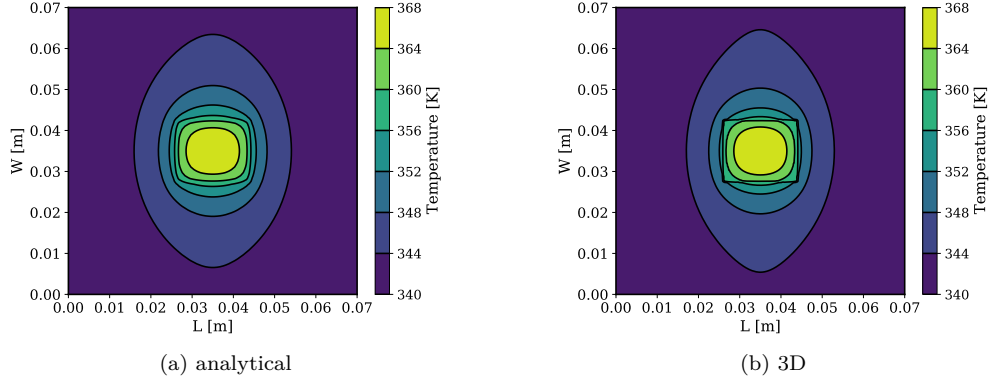
14

(a) analytical

(b) 3D

Figure 6: Case G - Isolines of temperature field [K] on top surface.

	$T_1\ [K]$	$R_t\ [K/W]$	$\bar{R}_t\ [K/W]$
analytical	367.84	1.484	1.250
3D	367.77	1.481	1.239

Table 8: Case G - Validation of the temperature peak and of the total component resistance results against solutions from three-dimensional simulations.

With respect to case F, the optimization procedure becomes here more complex, because of the two anisotropic layers. The application of the methodology to calculate the total resistance allows to plot Fig. 7a, from which the first layer optimal thickness can be extracted. The same holds for different values of the cross-plane conductivity of the first layer (Fig. 7b); the optimal first layer thickness varies with the cross-plane conductivity, even though the in-plane one does not change.

(a) constrained cross-plane conductivity

(b) variable cross-plane conductivity
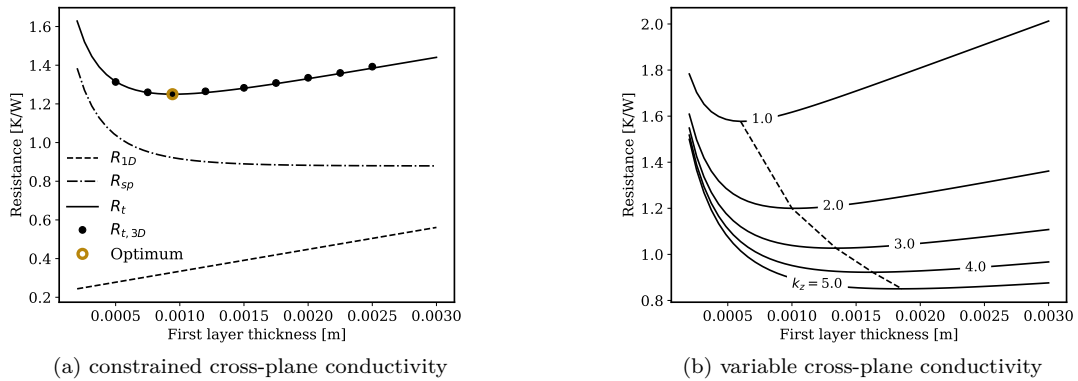
Figure 7: Case G - Minimization of total component resistance by optimization of first anisotropic layer thickness.

Again, multi-dimensional simulations have been carried out to validate the accuracy of the proposed solution and to calculate both the total component resistance and the peak temperature. The relative error in the peak temperature is always contained within 0.1% and the same holds for the total resistance (see Fig. 7a and 8). In order to decrease the total component resistance, the effects linked to three-dimensional heat spreading have

been also investigated. For a given thickness of the first substrate layer, a severe reduction in R_t is obtained if the cross-plane conductivity is increased. A reduction of the resistance $\Delta R_t \simeq 50\%$ is observed if larger values of $k_{z,1}$ are used ($k_{z,1} \to 10$ W/mK). This trend becomes progressively negligible for $k_{z,1} > 10$ W/mK. This result is supported by Fig. 5b. If the thickness of the first layer and the physical properties of the second layer are prescribed, the first layer spreading resistance is almost constant for $k_{z,1} \geq 10$ W/mK. Besides, the one-dimensional resistance of the first layer is marginally affected by a further increment of the cross-plane conductivity for this configuration. Plots of Fig. 8 are obtained with constant thicknesses as proposed in Tab. 6. However, it is proven the shift of the optimal thickness point for a change in layer conductivity. The dotted line of Fig. 7b reports the optimal thickness of the first layer for each configuration. The same can be seen in Fig. 9a. For the latter, the optimal thickness corresponds to the furthest to the left point of each iso-resistance curve.

(a) cross-plane   (b) in-plane
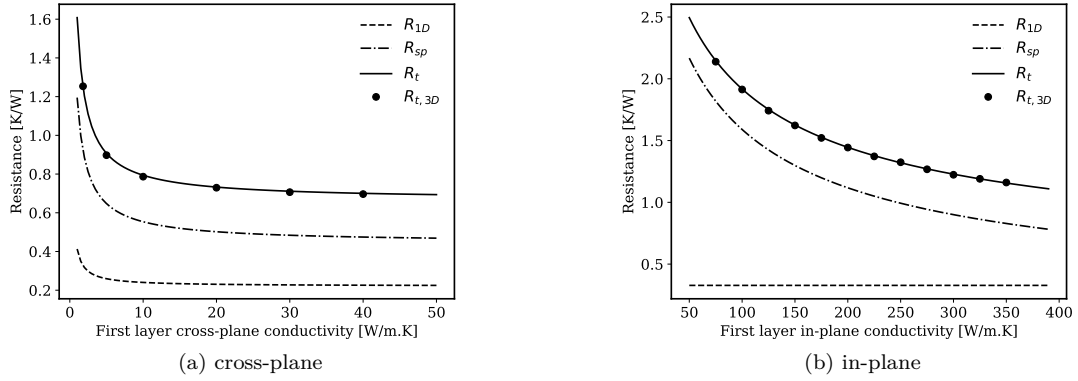
Figure 8: Case G - Total component resistance for variable thermal conductivity.

The behavior of total resistance is also studied for a conductivity variation along both in-plane directions in Fig. 9b. The performance is strongly influenced by the below anisotropic layer. Less effort is required to reduce the component resistance by increasing the first layer conductivity along y-direction, as $k_{x,2}$ is strongly limited. In order to similarly reduce the total resistance of the component by means of x-direction conductivity enhancement, one has to compensate for the small $k_{x,2}$ value of the second layer in the same direction.

(a) cross-plane   (b) in-plane

Figure 9: Case G - Isolines of total resistance for variable three-dimensional conductivity.

16

6.3. Multiple anisotropic layers with multiple components

The final test case is a multi-component configuration combined with a multi-layer anisotropic substrate. Four rectangular eccentric components of different dimensions are positioned to limit their reciprocal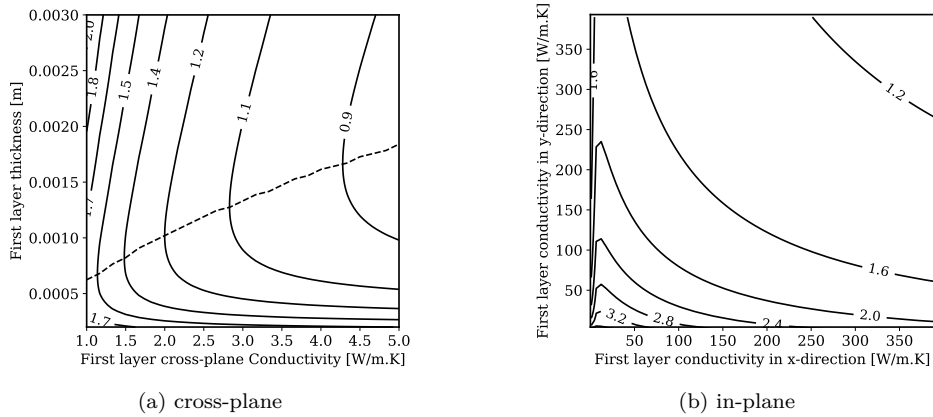 interaction (i.e. the total resistance of each component and its temperature peak). A schematic of the top-view of the system is reported in Fig. 1e, while the side-view of the substrate is shown in Fig. 1d. The components and substrate characteristics are described in Tab. 6. Isolines from the temperature field on the upper surface of the substrate are shown in Fig. 10 for validation. The agreement between three-dimensional simulations and the proposed method for the temperature field, the peak temperature and the total resistance (Tab. 9) is satisfying. Discrepancies are limited: $\text{err}_T < 0.1\%$, $\text{err}_{R_t} \simeq 0.1\%$, while the area averaged total resistance discrepancy is $\text{err}_{\bar{R}_t} \simeq 1\%$.
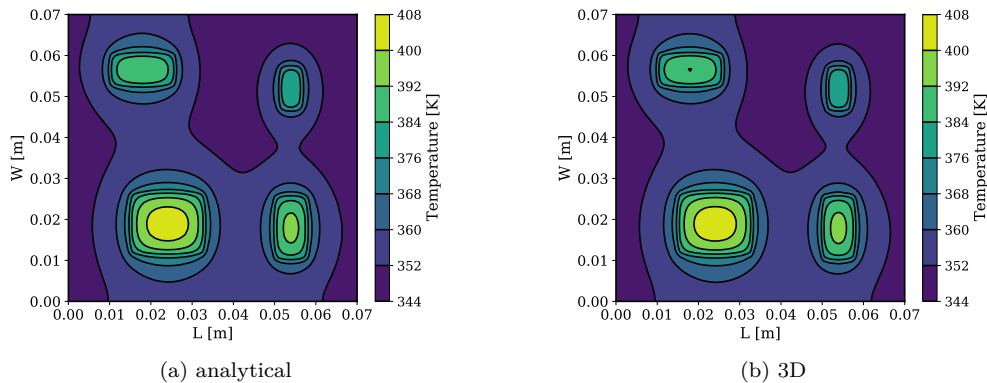

(a) analytical　　　　　　　　　　　(b) 3D

Figure 10: Case H - Isolines of temperature field [K] on top surface.

	$T_1\ [K]$	$\bar{R}_{t,1}\ [K/W]$	$T_2\ [K]$	$\bar{R}_{t,2}\ [K/W]$	$T_3\ [K]$	$\bar{R}_{t,3}\ [K/W]$	$T_4\ [K]$	$\bar{R}_{t,4}\ [K/W]$
analytical	404.70	2.776	394.69	4.771	392.01	4.609	384.03	7.842
3D	404.75	2.788	394.75	4.808	392.08	4.628	384.10	7.924

Table 9: Case H - Validation of the temperature peak and of the total component resistance results against solutions from three-dimensional simulations.

For this case, the optimization method is applied to both layers. Two constraints are set: each layer must have a minimum allowable thickness $t_{min} = 0.5$ mm and the maximum extent for the entire substrate is $t_{t,max} = t_1 + t_2 = 7$ mm. As a consequence, $t_t \in [1:7]$ mm. A procedure which minimizes the total resistance of each component is not feasible, because several sources are present in the system. Sec. 4 indicates how in these scenarios the minimization method aims at reducing the peak temperature on the upper surface. From Tab. 6, the conductivity of the upper layer of the substrate is lower than the below one cooled by the fluids. Also, the non-dimensional thickness ratio of the first layer is defined as:

$$\hat{t}_i = t_i/t_{t,max} \tag{39}$$

and for the initially proposed configuration, the first layer non-dimensional thickness is $\hat{t}_1 = t_1/t_{t,max} = 0.2857$. The optimizer varies the extent of one layer at a time. Fig. 11 shows the trend of the temperature peak for a variation of each layer thickness. In particular, the one of the first layer is varied in Fig. 11a considering a constant $t_2 = 5$ mm. The monotonic trend suggests that the first layer thickness must be reduced as much as possible. The same observation is derived from Fig. 11b where the evolution of temperature peak is reported for a variable second layer thickness provided a thin or thick first layer. By selecting $t_1 = 0.5$ mm, the maximum

end on the second layer is extended so that $t_2 \in [0.5 : 6.5]$. Without any other constraint, the optimal solution corresponds to $t_2 = 6.5$ mm, as the temperature behavior is monotonically decreasing as t_2 increases. If a constraint on the maximum weight is set, a coupling function should be considered (Sec. 4): the knowledge of weight per unit thickness would be sufficient to close the optimization process. Provided a thin top layer, Fig. 11b also points out that a large temperature decrement is obtained for a change in bottom layer thickness moving from t_2=0.5 mm to t_2= 3 mm. The gain for a variation from 3 mm to 6.5 mm is much more contained. Thus, even if a weight limitation were accounted, chances are that a sufficiently large reduction in surface peak temperature could be obtained.
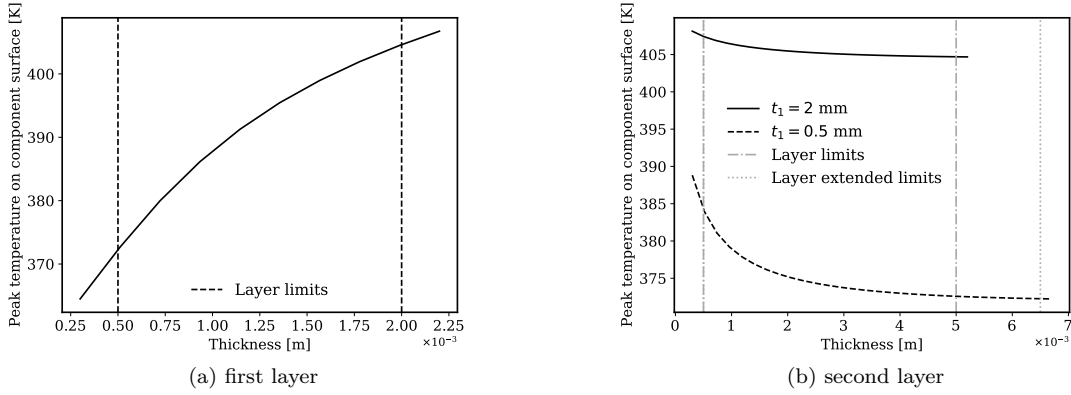
Figure 11: Case H - Peak temperature at top surface for variable thickness subjected to external constraints.

These observations are confirmed by the evolution of the peak temperature on the upper surface, that is plotted as the non-dimensional thickness of the first layer $\hat{t}_1$ varies (Fig. 12). The analysis is then repeated to show the solution with the new optimized thicknesses $\hat{t}_1 = 0.0714$. Results are in Fig. 13: the temperature peak for each component and the total component resistances are correctly captured. The discrepancies against the three-dimensional results are still limited (err $\simeq 0.1\%$).
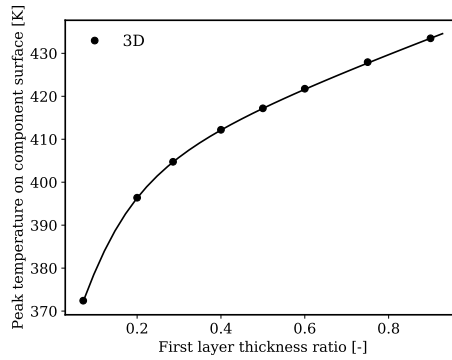
Figure 12: Case H - Peak temperature on the upper surface for different non-dimensional first layer thickness ratios $\hat{t}_1$.

18

(a) analytical

(b) 3D
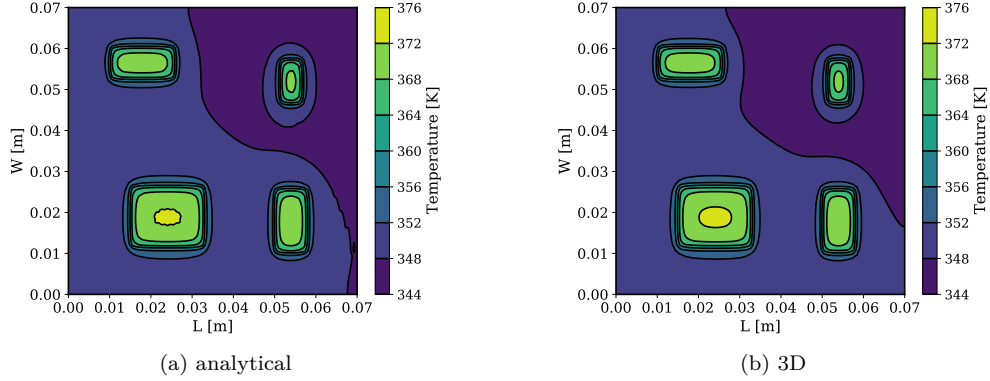
Figure 13: Optimized Case H - Isolines of temperature field [K] on top surface.

The presented optimization procedure reduces the temperature peak excess on the upper surface by 48.5% for this test case (see Tab. 10).

	$T_1\ [K]$	$\bar{R}_{t,1}\ [K/W]$	$T_2\ [K]$	$\bar{R}_{t,2}\ [K/W]$	$T_3\ [K]$	$\bar{R}_{t,3}\ [K/W]$	$T_4\ [K]$	$\bar{R}_{t,4}\ [K/W]$
analytical	372.38	1.521	371.27	2.883	370.25	2.835	368.98	5.315
3D	372.43	1.536	371.35	2.915	370.33	2.855	369.08	5.340

Table 10: Optimized Case H - Peak temperature excess is reduced by 48.5%.

(a) initial configuration

(b) optimized configuration
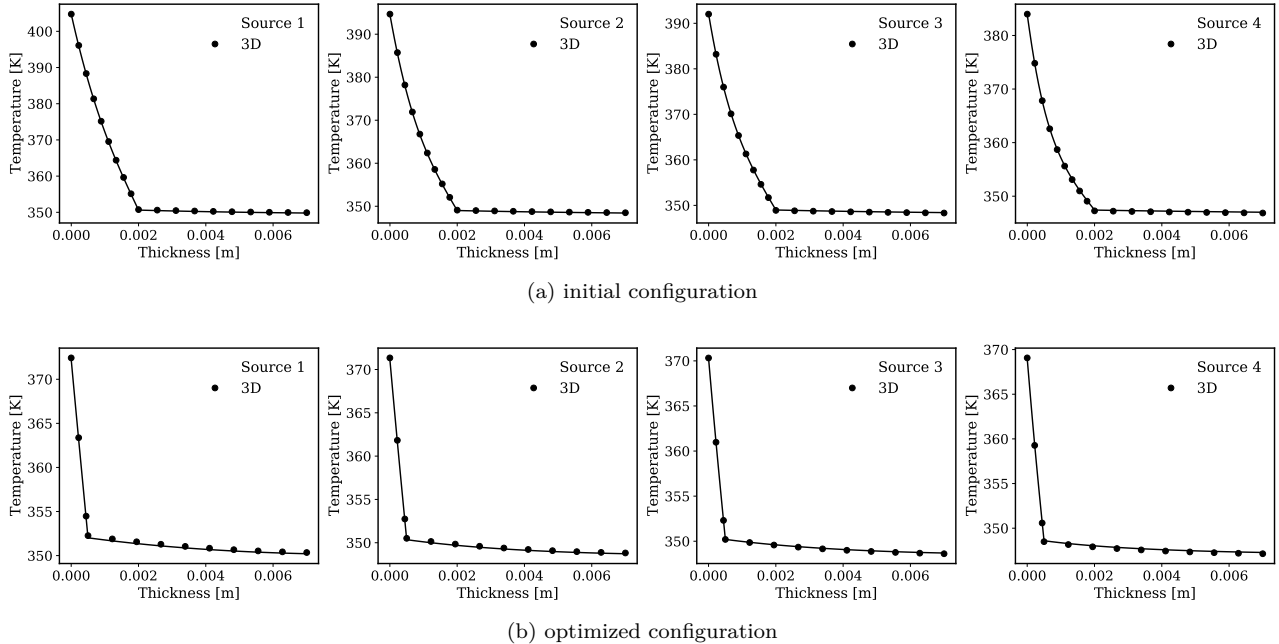
Figure 14: Optimized case H - Temperature evolution over a line crossing the substrate and passing through each component center.

Finally, from the theory of Sec. 2, the bi-dimensional in-plane temperature distribution is extracted along the thickness of every anisotropic layer. This implies the possibility to determine the temperature distribution over

19

a z-direction vertical line, provided the indication of a specific in-plane location. For instance, each line in Fig. 14 crosses the centroid of one component. The overall substrate behavior is correctly predicted by the proposed methodology (see Fig. 14). Fig. 14 also confirms that most of the thermal stress has to be appointed to the top layer, whose thickness reduction decreases and evens the temperature peak values.

7. Conclusions

The development of an algorithm to treat via analytical formulation the thermal problem in anisotropic compound systems with discrete heat sources is presented. The baseline approach includes the calculation of the thermal spreading in multi-component arrangements through the Influence Coefficient Method, that is able to predict the spreading resistance with very good accuracy. The methodology has proven to be able to quickly recover the simplified handling of single- and multi-component configurations on top of isotropic and orthotropic substrates with perfect interface adhesion or finite layer-to-layer conductance. These are configurations of high interest in Automotive, because of their good performance at a reduced cost. Moreover, to assert the applicability and repeatability of the approach for anisotropic substrates, results are validated against a series of three-dimensional multi-region simulations resembling realistic applications. When convective cooling is applied at the heat sink, experimental or semi-empirical correlations from literature properly estimate the heat transfer coefficient, avoiding expensive multi-region investigation. The proposed equations are used for a constrained automatic optimization procedure, where constraints are the maximum admissible weight, cost, and encumbrance, to minimize the temperature peak of the component or its resistance. Thermal spreading resistance can be reduced by investigating the effects of the heat transfer coefficient and of the Biot number. For an anisotropic multi-layer substrate with multiple heat sources, a reduction of the peak temperature excess up to 48.5% with respect to the baseline configuration is obtained. The analytical formulation is also able to predict the substrate thermal behavior for variable anisotropic conductivity. To reduce the substrate thermal stress, the heat spreading can be conveniently promoted along cross-plane and in-plane directions. The consequent thermal behavior of the system depends then on the type of substrate, on the heat power from the sources, and on the direction chosen for heat spreading promotion. All these aspects, together with the contraints related to the cost of the components, influence the solid layer optimal thickness. The proposed method and the described optimization steps lay the foundations for the development of an improved multi-variable optimizer to perform optimal relocation of the electrical components.

References

[1] Y. S. Muzychka, K. R. Bagnall, E. N. Wang, Thermal Spreading Resistance and Heat Source Temperature in Compound Orthotropic Systems With Interfacial Resistance, 44th AIAA Thermophysics Conference 3 (11) (2013) 1826–1841. `doi:10.1109/TCPMT.2013.2269273`.

[2] K. R. Bagnall, Y. S. Muzychka, E. N. Wang, Analytical Solution for Temperature Rise in Complex Multilayer Structures with Discrete Heat Sources, IEEE Transactions on Components, Packaging and Manufacturing Technology 4 (5) (2014) 817–830. `doi:10.1109/TCPMT.2014.2299766`.

[3] M. Garven, J. P. Calame, Simulation and Optimization of Gate Temperatures in GaN-on-SiC Monolithic Microwave Integrated Circuits, IEEE Transactions on Components and Packaging Technologies 32 (1) (2009) 63–72. `doi:10.1109/TCAPT.2008.2004586`.

[4] F. Bertoluzza, N. Delmonte, R. Menozzi, Three-dimensional finite-element thermal simulation of GaN-based HEMTs, Microelectronics Reliability 49 (5) (2009) 468 – 473, 2008 Reliability of Compound Semiconductors (ROCS) Workshop. `doi:10.1016/j.microrel.2009.02.009`.

[5] J. Ajayan, D. Nirmal, R. Ramesh, S. Bhattacharya, S. Tayal, L. Leo Joseph, L. Raju Thoutam, D. Ajitha, A critical review of AlGaN/GaN-heterostructure based Schottky diode/HEMT hydrogen (H2) sensors for aerospace and industrial applications, Measurement 186. `doi:10.1016/j.measurement.2021.110100`.

[6] D. Chen, J. Jiang, G.-H. Kim, C. Yang, A. Pesaran, Comparison of different cooling methods for lithium ion battery cells, Applied Thermal Engineering 94 (2016) 846–854. `doi:10.1016/j.applthermaleng.2015.10.015`.

[7] Z. An, L. Jia, Y. Ding, C. Dang, X. Li, A review on lithium-ion power battery thermal management technologies and thermal safety, Journal of Thermal Science 26 (5) (2017) 391–412. `doi:10.1007/s11630-017-0955-2`.

[8] C. Bibin, M. Vijayaram, V. Suriya, R. Sai Ganesh, S. Soundarraj, A review on thermal issues in Li-ion battery and recent advancements in battery thermal management system, Materials Today: Proceedings 33 (2020) 116–128. `doi:10.1016/j.matpr.2020.03.317`.

[9] A. Pesaran, Battery Thermal Management in EVs and HEVs: Issues and Solutions, Vol. 43, 2001, Advanced Automotive Battery Conference.

[10] A. Castelan, Modélisation de composants d'extraction de la chaleur: application à l'optimisation de système d'électronique de puissance, Ph.D. thesis, Université Paul Sabatier - Toulouse III (Dec. 2017). URL `https://tel.archives-ouvertes.fr/tel-02004318/file/2017TOU3bis.pdf`

[11] G. Patankar, J. A. Weibel, S. V. Garimella, A validated time-stepping analytical model for 3D transient vapor chamber transport, International Journal of Heat and Mass Transfer 119 (2018) 867–879. `doi:10.1016/j.ijheatmasstransfer.2017.11.135`.

[12] C. Song, J. Kim, J. Cho, The effect of GaN epilayer thickness on the near-junction thermal resistance of GaN-on-diamond devices, International Journal of Heat and Mass Transfer 158. `doi:10.1016/j.ijheatmasstransfer.2020.119992`.

[13] A. Kokkas, Thermal analysis of multiple-layer structures, IEEE Transactions on Electron Devices 21 (11) (1974) 674–681. `doi:10.1109/T-ED.1974.17993`.

[14] M. M. Yovanovich, Y. S. Muzychka, J. R. Culham, Spreading resistance of isoflux rectangles and strips on compound flux channels, Journal of thermophysics and heat transfer 13 (4) (1999) 495–500. `doi:10.2514/2.6467`.

[15] K. Choudhury, D. Rogers, Steady-State Thermal Modeling of a Power Module: An N-Layer Fourier Approach, IEEE Transactions on Power Electronics PP. `doi:10.1109/TPEL.2018.2828439`.

[16] B. Subedi, S. H. Kim, S. P. Jang, M. A. Kedzierski, Effect of mesh wick geometry on the maximum heat transfer rate of flat-micro heat pipes with multi-heat sources and sinks, International Journal of Heat and Mass Transfer 131 (2019) 537–545. `doi:10.1016/j.ijheatmasstransfer.2018.11.086`.

[17] M. Razavi, Y. S. Muzychka, S. Kocabiyik, Review of advances in thermal spreading resistance problems, Journal of Thermophysics and Heat Transfer 30 (4) (2016) 863–879. `doi:10.2514/1.T4801`.

[18] T. Q. Feng, J. L. Xu, An analytical solution of thermal resistance of cubic heat spreaders for electronic cooling, Applied Thermal Engineering 24 (2-3) (2004) 323–337. `doi:10.1016/j.applthermaleng.2003.07.001`.

[19] S. M. Thompson, H. B. Ma, C. W. LaPierre, Thermal spreading analysis of rectangular heat spreader, Journal of Heat Transfer 136 (6) (2014) 1–8. `doi:10.1115/1.4026558`.

[20] Y. S. Muzychka, M. M. Yovanovich, J. R. Culham, Influence of Geometry and Edge Cooling on Thermal Spreading Resistance, Journal of Thermophysics and Heat Transfer 20 (2) (2006) 247–255. `doi:10.2514/1.14807`.

[21] J. Zhang, H. Yan, Y. Li, P. Niu, Q. Yang, An analytical model of thermal performance for an eccentric heat source on a rectangular plate with double-sided convective cooling, AIP Advances 9 (2) (2019) 025002. `doi:10.1063/1.5080771`.

[22] Y. S. Muzychka, J. R. Culham, M. M. Yovanovich, Thermal spreading resistance of eccentric heat sources on rectangular flux channels, Journal of Electronic Packaging, Transactions of the ASME 125 (2 SPEC.) (2003) 178–185. `doi:10.1115/1.1568125`.

[23] Y. S. Muzychka, M. M. Yovanovich, J. R. Culham, Application of thermal spreading resistance in compound and orthotropic systems, 39th Aerospace Sciences Meeting and Exhibit`doi:10.2514/6.2001-366`.

[24] Y. S. Muzychka, M. M. Yovanovich, J. R. Culham, Thermal spreading resistance in compound and orthotropic systems, Journal of Thermophysics and Heat Transfer 18 (1) (2004) 45–51. `doi:10.2514/1.1267`.

[25] B. Al-Khamaiseh, Y. S. Muzychka, S. Kocabiyik, Spreading resistance in multilayered orthotropic flux channel with temperature-dependent thermal conductivities, Journal of Thermophysics and Heat Transfer 32 (2) (2018) 392–400. `doi:10.2514/1.T5337`.

[26] A. Gholami, M. Bahrami, Thermal spreading resistance inside anisotropic plates with arbitrarily located hotspots, Journal of Thermophysics and Heat Transfer 28 (4) (2014) 679–686. `doi:10.2514/1.T4428`.

[27] Y.-S. Chen, K.-H. Chien, C.-C. Wang, T.-C. Hung, Y.-M. Ferng, B.-S. Pei, Investigations of the Thermal Spreading Effects of Rectangular Conduction Plates and Vapor Chamber, Journal of Electronic Packaging 129 (3) (2006) 348–355. `doi:10.1115/1.2753970`.

[28] J. Velardo, A. Date, R. Singh, J. Nihill, A. Date, T. L. Phan, On the effective thermal conductivity of the vapour region in vapour chamber heat spreaders, International Journal of Heat and Mass Transfer 145. `doi:10.1016/j.ijheatmasstransfer.2019.118797`.

[29] K. Zeghari, H. Louahlia, Flat miniature heat pipe with sintered porous wick structure: experimental and mathematical studies., International Journal of Heat and Mass Transfer 158. `doi:10.1016/j.ijheatmasstransfer.2020.120021`.

[30] H. K. Yun, Y. K. Seo, H. R. Gwang, Evaluation of spreading thermal resistance for heat generating multi-electronic components, Thermomechanical Phenomena in Electronic Systems - Proceedings of the Intersociety Conference (2006) 258–264. `doi:10.1109/ITHERM.2006.1645351`.

[31] Y. S. Muzychka, Influence Coefficient Method for calculating discrete heat source temperature on finite convectively cooled substrates, IEEE Transactions on Components and Packaging Technologies 29 (3) (2006) 636–643. `doi:10.1109/TCAPT.2006.880477`.

[32] D. Schweitzer, L. Chen, Heat spreading revisited - Effective heat spreading angle, Annual IEEE Semiconductor Thermal Measurement and Management Symposium 2015-April (2015) 88–94. `doi:10.1109/SEMI-THERM.2015.7100145`.

[33] G. Maranzana, I. Perry, D. Maillet, S. Raël, Design optimization of a spreader heat sink for power electronics, International Journal of Thermal Sciences 43 (1) (2004) 21–29. `doi:10.1016/S1290-0729(03)00107-8`.

[34] Y. S. Chen, K. H. Chien, Y. S. Tseng, Y. K. Chan, Determination of optimized rectangular spreader thickness for lower thermal spreading resistance, Journal of Electronic Packaging, Transactions of the ASME 131. `doi:10.1115/1.3068299`.

[35] Y. Peles, A. Koşar, C. Mishra, C. J. Kuo, B. Schneider, Forced convective heat transfer across a pin fin micro heat sink, International Journal of Heat and Mass Transfer 48 (17) (2005) 3615–3627. `doi:10.1016/j.ijheatmasstransfer.2005.03.017`.

[36] S. Luhar, D. Sarkar, A. Jain, Steady state and transient analytical modeling of non-uniform convective cooling of a microprocessor chip due to jet impingement, International Journal of Heat and Mass Transfer 110 (2017) 768–777. `doi:10.1016/j.ijheatmasstransfer.2017.03.064`.

[37] S. W. Churchill, M. Bernstein, A correlating equation for forced convection from gases and liquids to a circular cylinder in crossflow, Journal of Heat Transfer 99 (2) (1977) 300–306. `doi:10.1115/1.3450685`.

[38] A. Žukauskas, R. Ulinskas, Efficiency parameters for heat transfer in tube banks, Heat Transfer Engineering 6 (1) (1985) 19–25. doi:10.1080/01457638508939614.

[39] W. A. Khan, Modeling of Fluid Flow and Heat Transfer for Optimization of Pin-Fin Heat Sinks, University of Waterloo.
URL http://hdl.handle.net/10012/947

[40] J. P. Holman, Heat Transfer, 10th Edition, McGraw-Hill Series in Mechanical Engineering, 2009.

[41] M. Razavi, Y. S. Muzychka, S. Kocabiyik, Thermal Resistance in a Rectangular Flux Channel with Nonuniform Heat Convection in the Sink Plane, Journal of Heat Transfer 137 (11) (2015) 1–9. doi:10.1115/1.4030885.

[42] The OpenFOAM Foundation. [link].
URL http://www.openfoam.org/dev.php

[43] J. H. Ferziger, M. Perić, R. L. Street, Computational Methods for Fluid Dynamics, 4th Edition, Springer, 2020.

A. Analytical isotropic simplification

Isotropic solid materials have uniform thermal conductivity ($k_x = k_y = k_z$). Hence, starting from Eq. 10, the general expression for the temperature excess is:

$$\theta = A_{00} + B_0 z + \sum_{m=1}^{\infty} \cos(\lambda_m x) \left[A_m \, \cosh(\lambda_m z) + B_m \, \sinh(\lambda_m z) \right]$$

$$+ \sum_{n=1}^{\infty} \cos(\delta_n y) \left[A_n \, \cosh(\delta_n z) + B_n \, \sinh(\delta_n z) \right]$$

$$+ \sum_{m=1}^{\infty} \sum_{n=1}^{\infty} \cos(\lambda_m x) \cos(\delta_n y) \left[A_{mn} \, \cosh(\beta_{mn} z) + B_{mn} \, \sinh(\beta_{mn} z) \right] \tag{40}$$

where $\lambda_m = \dfrac{m\pi}{L}$, $\delta_n = \dfrac{n\pi}{W}$ and $\beta_{mn} = \sqrt{\lambda_m^2 + \delta_n^2}$. The equation which describes the two-dimensional temperature distribution over the top surface of the solid substrate is a simplification of Eq. 40:

$$\theta|_{z_1=0} = A_{00} + \sum_{m=1}^{\infty} A_m \cos(\lambda_m x) + \sum_{n=1}^{\infty} A_n \cos(\delta_n y) + \sum_{m=1}^{\infty} \sum_{n=1}^{\infty} A_{mn} \cos(\lambda_m x) \cos(\delta_n y) \tag{41}$$

Moreover, by link of Eq. 40 with the boundary condition proposed in Eq. 7, it follows:

$$B_0 = -\left(\frac{\bar{h}}{k_N + \bar{h} t_N} \right) A_{00} \tag{42}$$

$$B_{i,N} = -\left(\frac{\bar{h} + k_N \gamma \tanh(\gamma t_N)}{\bar{h} \tanh(\gamma t_N) + k_N \gamma} \right) A_{i,N} = -\Phi_N(\gamma) A_{i,N} \tag{43}$$

with $\gamma = \lambda_m, \, \delta_n, \, \beta_{mn}$ for $B_i = B_m, \, B_n, \, B_{mn}$ respectively.

As expressed in Sec. 2, system closure can be obtained thanks to different set of boundary conditions for different layer-to-layer interfaces. For *perfect adhesion* see Eq. 13 and 14, while for *finite conductance* refer to Eq. 21 and 22.

A.1. Perfect adhesion

For multi-layer scenarios with *perfect adhesion* between layers, each layer $j \in [1 : N-1]$ is characterized by:

$$B_{i,j} = -\left(\frac{\tanh(\gamma t_j) + \Phi_{j+1}(\gamma) \frac{k_{j+1}}{k_j}}{1 + \Phi_{j+1}(\gamma) \frac{k_{j+1}}{k_j} \tanh(\gamma t_j)} \right) A_{i,j} = -\Phi_j(\gamma) A_{i,j} \tag{44}$$

Each B_i calculation serves for the determination of the A_i values, by combination with Eq. 5:

$$A_{00} = \frac{Q}{LW} \left(\sum_{j=1}^{N} \frac{t_j}{k_j} + \frac{1}{\bar{h}} \right) \tag{45}$$

$$A_m = \sum_{m=1}^{\infty} \frac{4Q \cos(\lambda_m X_c) \sin\left(\lambda_m \frac{L_c}{2}\right)}{LW L_c \, k_j \lambda_m^2 \Phi(\lambda)} \tag{46}$$

$$A_n = \sum_{n=1}^{\infty} \frac{4Q \cos(\delta_n Y_c) \sin\left(\delta_n \frac{W_c}{2}\right)}{LW W_c \, k_j \delta_n^2 \Phi(\delta)} \tag{47}$$

$$A_{mn} = \sum_{m=1}^{\infty} \sum_{n=1}^{\infty} \frac{16Q \cos(\lambda_m X_c) \cos(\delta_n Y_c) \sin\left(\lambda_m \frac{L_c}{2}\right) \sin\left(\delta_n \frac{W_c}{2}\right)}{LW L_c W_c \, k_j \, \lambda_m \delta_n \beta_{mn} \, \Phi(\beta)} \tag{48}$$

A.2. Finite conductance over layer-to-layer interface

For isotropic layers having *finite conductance* the spreading function $\Phi_j(\gamma)$ is largely simplified. In particular, for each solid sheet $j \in [1 : N-1]$ the following is valid:

$$B_{i,j} = -\left(\frac{\frac{k_j}{k_{j+1}}\tanh\left(\gamma t_j\right) + \Phi_{j+1}(\gamma)\frac{k_j}{h_{f,j}}\gamma\tanh\left(\gamma t_j\right) + \Phi_{j+1}(\gamma)}{\frac{k_j}{k_{j+1}} + \Phi_{j+1}(\gamma)\frac{k_j}{h_{f,j}}\gamma + \Phi_{j+1}(\gamma)\tanh\left(\gamma t_j\right)}\right)A_{i,j} = -\Phi_j(\gamma)A_{i,j} \tag{49}$$

In these configurations the A_{00} value changes as well, becoming:

$$A_{00} = \frac{Q}{LW}\left(\frac{1}{\bar{h}} + \sum_{j=1}^{N-1}\frac{1}{h_{f,j}} + \sum_{j=1}^{N}\frac{t_j}{k_j}\right) \tag{50}$$

Finally, the isotropic equation which characterizes the area averaged temperature excess is simplified with respect to its anisotropic counterpart (Eq. 31). Nevertheless, the following is valid for cases having either perfect layer-to-layer adhesion, or finite conductance at the interface. For the i-th component effect on s-th heat source (and its respective centroid position), one has:

$$\bar{\theta}_s|_{z_1=0} = A_{00} + \sum_{m=1}^{\infty}A_{m,i}\frac{2\cos\left(\lambda_m X_{c,s}\right)\sin\left(\lambda_m\frac{L_{c,s}}{2}\right)}{\lambda_m L_{c,s}} + \sum_{n=1}^{\infty}A_{n,i}\frac{2\cos\left(\delta_n Y_{c,s}\right)\sin\left(\delta_n\frac{W_{c,s}}{2}\right)}{\delta_n W_{c,s}}$$

$$+ \sum_{m=1}^{\infty}\sum_{n=1}^{\infty}A_{mn,i}\frac{4\cos\left(\lambda_m X_{c,s}\right)\sin\left(\lambda_m\frac{L_{c,s}}{2}\right)\cos\left(\delta_n Y_{c,s}\right)\sin\left(\delta_n\frac{W_{c,s}}{2}\right)}{\lambda_m\delta_n L_{c,s}W_{c,s}} \tag{51}$$

The required A_i values are presented in Eq. 46 to 48, and A_{00} is either the one of Eq. 45 or Eq. 50. The equations specifically derived for the isotropic case are consistent with the literature [2, 18, 19, 22].

B. Analytical orthotropic simplification

Orthotropic solid materials are oriented to have a uniform in-plane conduction, which differs from the cross-plane one ($k_x = k_y = k_{ip} \neq k_z$). Thus, knowing Eq. 10, the expression for the temperature excess is simplified into:

$$\theta = A_{00} + B_0\sqrt{\frac{k_{ip}}{k_z}}z$$

$$+ \sum_{m=1}^{\infty}\cos(\lambda_m x)\left[A_m\,\cosh\left(\lambda_m\sqrt{\frac{k_{ip}}{k_z}}z\right) + B_m\,\sinh\left(\lambda_m\sqrt{\frac{k_{ip}}{k_z}}z\right)\right]$$

$$+ \sum_{n=1}^{\infty}\cos\left(\delta_n y\right)\left[A_n\,\cosh\left(\delta_n\sqrt{\frac{k_{ip}}{k_z}}z\right) + B_n\,\sinh\left(\delta_n\sqrt{\frac{k_{ip}}{k_z}}z\right)\right]$$

$$+ \sum_{m=1}^{\infty}\sum_{n=1}^{\infty}\cos(\lambda_m x)\cos\left(\delta_n y\right)\left[A_{mn}\,\cosh\left(\beta_{mn}\sqrt{\frac{k_{ip}}{k_z}}z\right) + B_{mn}\,\sinh\left(\beta_{mn}\sqrt{\frac{k_{ip}}{k_z}}z\right)\right] \tag{52}$$

where $\lambda_m = \dfrac{m\pi}{L}$, $\delta_n = \dfrac{n\pi}{W}$ and $\beta_{mn} = \sqrt{\lambda_m^2 + \delta_n^2}$. Starting from Eq. 52, the two-dimensional temperature excess distribution is described on top surface by Eq. 41, but some differences are present in the spreading function evaluation, which in turn affect the A_i values.

By connection of Eq. 52 with the boundary condition of Eq. 7, one has:

$$B_0 = -\left(\frac{\bar{h}}{k_{z,N} + \bar{h}t_N}\right)\sqrt{\frac{k_{z,N}}{k_{ip,N}}}\,A_{00} \tag{53}$$

$$B_{i,N} = -\left(\frac{\bar{h} + k_{z,N}\gamma\sqrt{\frac{k_{ip,N}}{k_{z,N}}}\tanh\left(\gamma\sqrt{\frac{k_{ip,N}}{k_{z,N}}}t_N\right)}{\bar{h}\tanh\left(\gamma\sqrt{\frac{k_{ip,N}}{k_{z,N}}}t_N\right) + k_{z,N}\gamma\sqrt{\frac{k_{ip,N}}{k_{z,N}}}}\right)A_{i,N} = -\Phi_N(\gamma)A_{i,N} \tag{54}$$

with $\gamma = \lambda_m,\ \delta_n,\ \beta_{mn}$ for $B_i = B_m,\ B_n,\ B_{mn}$ respectively.

The closure equations are based on the different set of boundary conditions, as expressed in Sec. 2. For *perfect adhesion* see Eq. 13 and 14, and for *finite conductance* refer to Eq. 21 and 22.

B.1. Perfect adhesion

For multi-layer configurations subjected to *perfect adhesion*, the following expression is valid for each layer $j \in [1:N-1]$:

$$B_{i,j} = -\left(\frac{\tanh\left(\gamma\sqrt{\frac{k_{ip,j}}{k_{z,j}}}t_j\right) + \Phi_{j+1}(\gamma)\sqrt{\frac{k_{z,j+1}}{k_{z,j}}}\sqrt{\frac{k_{ip,j+1}}{k_{ip,j}}}}{1 + \Phi_{j+1}(\gamma)\sqrt{\frac{k_{z,j+1}}{k_{z,j}}}\sqrt{\frac{k_{ip,j+1}}{k_{ip,j}}}\tanh\left(\gamma\sqrt{\frac{k_{ip,j}}{k_{z,j}}}t_j\right)}\right)A_{i,j} = -\Phi_j(\gamma)A_{i,j} \tag{55}$$

Also, from Eq. 5 it follows:

$$A_{00} = \frac{Q}{LW}\left(\sum_{j=1}^{N}\frac{t_j}{k_{z,j}} + \frac{1}{\bar{h}}\right) \tag{56}$$

$$A_m = \sum_{m=1}^{\infty}\frac{4Q\cos\left(\lambda_m X_c\right)\sin\left(\lambda_m\frac{L_c}{2}\right)}{LWL_c\ k_{z,j}\lambda_m^2\Phi(\lambda)\sqrt{\frac{k_{ip,j}}{k_{z,j}}}} \tag{57}$$

$$A_n = \sum_{n=1}^{\infty}\frac{4Q\cos\left(\delta_n Y_c\right)\sin\left(\delta_n\frac{W_c}{2}\right)}{LWW_c\ k_{z,j}\delta_n^2\Phi(\delta)\sqrt{\frac{k_{ip,j}}{k_{z,j}}}} \tag{58}$$

$$A_{mn} = \sum_{m=1}^{\infty}\sum_{n=1}^{\infty}\frac{16Q\cos\left(\lambda_m X_c\right)\cos\left(\delta_n Y_c\right)\sin\left(\lambda_m\frac{L_c}{2}\right)\sin\left(\delta_n\frac{W_c}{2}\right)}{LWL_cW_c\ k_{z,j}\ \lambda_m\delta_n\beta_{mn}\ \Phi(\beta)\sqrt{\frac{k_{ip,j}}{k_{z,j}}}} \tag{59}$$

B.2. Finite conductance over layer-to-layer interface

The spreading function $\Phi_j(\gamma)$ of orthotropic substrates subjected to *finite conductance* slightly varies. The equation describing it for the layer $j \in [1:N-1]$ becomes:

$$B_{i,j} = -\underbrace{\left(\frac{\frac{k_{z,j}}{k_{z,j+1}}\tanh\left(\gamma\sqrt{\frac{k_{ip,j}}{k_{z,j}}}t_j\right) + \Phi_{j+1}(\gamma)\frac{k_{z,j}}{h_{f,j}}\gamma\sqrt{\frac{k_{ip,j+1}}{k_{z,j+1}}}\tanh\left(\gamma\sqrt{\frac{k_{ip,j}}{k_{z,j}}}t_j\right) + \Phi_{j+1}(\gamma)\sqrt{\frac{k_{ip,j+1}}{k_{z,j+1}}}\sqrt{\frac{k_{z,j}}{k_{ip,j}}}}{\frac{k_{z,j}}{k_{z,j+1}} + \Phi_{j+1}(\gamma)\frac{k_{z,j}}{h_{f,j}}\gamma\sqrt{\frac{k_{ip,j+1}}{k_{z,j+1}}} + \Phi_{j+1}(\gamma)\sqrt{\frac{k_{ip,j+1}}{k_{z,j+1}}}\sqrt{\frac{k_{z,j}}{k_{ip,j}}}\tanh\left(\gamma\sqrt{\frac{k_{ip,j}}{k_{z,j}}}t_j\right)}\right)}_{\Phi_j(\gamma)}A_{i,j}$$

$$\tag{60}$$

The A_{00} value for finite conductance cases is identical to the anisotropic one of Eq. 16.

The orthotropic equation defining the area averaged temperature excess over the source plane has the same expression of Eq. 51, but the orthotropic A_i terms must be used. They are presented in Eq. 57 to 59. The expression of A_{00} is the same of Eq. 16 and Eq. 56. The equations specifically derived for the orthotropic case are consistent with the literature [1, 25].

C. Fixed temperature boundary condition

An average heat transfer coefficient $\bar{h} \to \infty$ is applied at the bottom of the N-th layer in cases C and D of Tab. 1. This represents a constant temperature boundary condition. To prove this assumption for anisotropic substrates, Eq. 7 is replaced with the following homogeneous equation:

$$\theta_N = A_{00} + B_0 \sqrt{\frac{k_{x,N}}{k_{z,N}}} t_N + \sum_{m=1}^{\infty} \cos(\lambda_m x) \left[A_m \cosh\left(\lambda_m \sqrt{\frac{k_{x,N}}{k_{z,N}}} t_N \right) + B_m \sinh\left(\lambda_m \sqrt{\frac{k_{x,N}}{k_{z,N}}} t_N \right) \right]$$
$$+ \sum_{n=1}^{\infty} \cos\left(\delta_n \sqrt{\frac{k_{x,N}}{k_{y,N}}} y \right) \left[A_n \cosh\left(\delta_n \sqrt{\frac{k_{x,N}}{k_{z,N}}} t_N \right) + B_n \sinh\left(\delta_n \sqrt{\frac{k_{x,N}}{k_{z,N}}} t_N \right) \right]$$
$$+ \sum_{m=1}^{\infty} \sum_{n=1}^{\infty} \cos(\lambda_m x) \cos\left(\delta_n \sqrt{\frac{k_{x,N}}{k_{y,N}}} y \right) \left[A_{mn} \cosh\left(\beta_{mn} \sqrt{\frac{k_{x,N}}{k_{z,N}}} t_N \right) + B_{mn} \sinh\left(\beta_{mn} \sqrt{\frac{k_{x,N}}{k_{z,N}}} t_N \right) \right] = 0 \tag{61}$$

Eq. 61 provides:

$$A_{00} = -B_0 \sqrt{\frac{k_{x,N}}{k_{z,N}}} t_N \tag{62}$$

For single layer substrates, from Eq. 5 one gets:

$$B_0 = -\frac{Q}{LW k_{z,N}} \sqrt{\frac{k_{z,N}}{k_{x,N}}} \tag{63}$$

thus making:

$$A_{00} = \frac{Q}{LW} \frac{t_N}{k_{z,N}} \tag{64}$$

Alternatively, for multilayer packs with perfect layer adhesion (Eq. 13 and 14) one has:

$$A_{00} = \frac{Q}{LW} \left(\sum_{j=1}^{N} \frac{t_j}{k_{z,j}} \right) \tag{65}$$

And for multilayer packs with finite conductance at the layer-to-layer interface, the following is valid:

$$A_{00} = \frac{Q}{LW} \left(\sum_{j=1}^{N-1} \frac{1}{h_{f,j}} + \sum_{j=1}^{N} \frac{t_j}{k_{z,j}} \right) \tag{66}$$

The spreading functions for the upper layers $\Phi_j(\gamma)$ are unchanged compared to Eq. 15; the spreading function of the bottom layer $\Phi_N(\gamma)$ becomes:

$$\Phi_N(\gamma) = \frac{1}{\tanh\left(\gamma \sqrt{\frac{k_{x,N}}{k_{z,N}}} t_N \right)} \tag{67}$$

where $\gamma = \lambda_m, \delta_n$ and β_{mn}.

These equations can be obtained by imposing $\bar{h} \to \infty$ into Eq. 11, 12 and 16 (or 24). Thus, when $\bar{h} \to \infty$ a constant temperature BC is applied at the bottom of the substrate.